

Integrating b -Value and Background Seismicity Rate for Spatial Earthquake Forecasting in the Alborz Region, Northern Iran

Muhammed Hossein Mousavi ¹, Hamzeh Mohammadigheymasi ^{2,3}, Parva Sadeghi Alavijeh ⁴, Marjan Tourani ⁵

¹Department of Physics Education, Farhangian University, Tehran, Iran, ²Atmosphere and Ocean Research Institute (AORI), The University of Tokyo, Kashiwa, Japan, ³Department of Computer Sciences, University of Beira Interior, Covilha, Portugal, ⁴Department of Physics, University of Kashan, Kashan, Iran, ⁵Department of Geological Engineering, Ankara University, Tectonics Research Group, Ankara, Türkiye

Abstract In this study, we evaluate the spatial forecasting skill of the b -value and background seismicity rate μ across the Alborz region using a homogenized catalog of 23,961 earthquakes ($M \geq 1.5$) recorded by the Iranian Seismological Center between 2006 and 2024. Forecast performance for $M \geq 4.0$ and $M \geq 4.5$ is assessed using Molchan error diagrams, probability gain, probability difference, and the modified area skill score. The results show that μ provides a consistently strong spatial signal, with Molchan curves well below the random baseline and probability gains of 5–6 at low alarm rates, reflecting the persistent clustering of seismicity along major Alborz faults. The b -value exhibits limited skill at lower magnitudes but improves steadily with increasing magnitude; its skill score becomes positive above $M \approx 5.3$, indicating that b -value anomalies begin to capture meaningful stress concentrations only for larger events. Spatial patterns reveal low b zones along active reverse and strike-slip structures and high μ zones following long-term seismicity clusters, underscoring their complementary physical roles. Retrospective testing confirms this complementarity: the combined b - μ forecast achieves detection rates of 0.81–0.83 at spatial alarm rates of 0.43 and 0.36 for $M \geq 4.0$ and $M \geq 4.5$, respectively, representing the most efficient forecast configuration among all tested models. These findings demonstrate that integrating stress-state and tectonic-loading indicators yields a more efficient and physically grounded framework for operational earthquake forecasting in the Alborz region.

Non-technical summary Earthquakes are a major hazard in northern Iran's active Alborz region. To improve forecasting, we analyzed nearly 24,000 earthquakes recorded between 2006 and 2024, evaluating two geological indicators: the background seismicity rate, which tracks tectonic loading, and the b value, representing deep crustal stress. We found that the background seismicity rate is a highly stable spatial predictor across all magnitudes, as earthquakes naturally cluster along active faults. In contrast, the stress sensitive b value is less informative for minor tremors but becomes a powerful forecasting tool for larger, potentially damaging earthquakes (magnitude 5.3 and above) as faults approach their breaking point. Because these indicators track complementary physical processes, representing ongoing tectonic loading versus current structural pressure,

combining them into a unified forecast outperforms either tool used alone. This integrated model successfully anticipates over 80% of moderate to large earthquakes while minimizing false alarms. Our study offers a testable forward looking hazard map for 2025 to 2029, establishing a stronger, physically grounded foundation for disaster mitigation and seismic risk reduction in active mountain belts.

1 Introduction

Earthquakes are among the most destructive natural hazards on Earth, capable of collapsing buildings, severing lifelines, and disrupting the social and economic fabric of entire communities for years or decades after the event [Kazama and Noda \(2012\)](#); [Cui et al. \(2011\)](#). The 2004 M_w 9.0 Sumatra, 2008 M_w 8.0 Wenchuan, and 2010 M_w 7.0 Haiti earthquakes each illustrated, across very different tectonic and societal settings, how comprehensively a single rupture can reshape the trajectory of entire nations [Nanjo et al. \(2012\)](#); [Shi et al. \(2018\)](#); [Cavallo et al. \(2010\)](#). The desire to anticipate such events before they occur has motivated earthquake forecasting research for much of the past century, even as that research has required, as [Jordan and Jones \(2010\)](#) and [Geller et al. \(1997\)](#) have frankly acknowledged, repeated reassessment of what the field can and cannot deliver. The methods brought to bear on this problem have been remarkably diverse. Seismic gap analysis, characteristic earthquake models, static and dynamic stress transfer, aftershock sequence modeling, pattern recognition, and more recently machine learning have all contributed to our understanding of how and where earthquakes occur [Bakun and Lindh \(1985\)](#); [King et al. \(1994\)](#); [Brodsky \(2006\)](#); [Keilis-Borok and Kossobokov \(1990\)](#); [Wang et al. \(2004\)](#). Yet reliable intermediate- to long-term forecasting across tectonically complex regions remains a significant scientific challenge. Classical models were largely developed for the sparser catalogs of earlier monitoring eras and have not always kept pace with the richer datasets now available, while the fundamental rarity of large damaging earthquakes continues to limit the statistical power of any validation exercise [Jordan and Jones \(2010\)](#); [Michael et al. \(2020\)](#); [Beroza et al. \(2021\)](#). Against this background, the Gutenberg–Richter b -value has established itself as one of the most physically meaningful and operationally tractable indicators of seismic potential [Gutenberg and Richter \(1944\)](#). Its utility for hazard assessment lies not simply in this descriptive role but in its sensitivity to crustal stress: both laboratory experiments and field studies have consistently shown that b -values decrease as differential stress increases and rise where the crust is more heterogeneous or heavily fractured [Scholz \(2015\)](#); [Beall et al. \(2022\)](#). This physical relationship gives spatial b -value variations genuine diagnostic power. Anomalously low b -values were documented in the epicentral regions of the 2004 Sumatra, 2008 Wenchuan, and 2011 Tohoku earthquakes prior to their occurrence [Nanjo et al. \(2012\)](#); [El-Isa and Eaton \(2014\)](#); [Shi et al. \(2018\)](#), lending empirical support to the interpretation that b -value mapping can track where fault systems may be approaching failure. Natural time analyses have extended this picture further, connecting pre-mainshock b -value decreases to critical state dynamics in the evolving seismic system [Sarlis et al. \(2015\)](#); [Nanjo et al. \(2022\)](#); [Convertito et al. \(2024\)](#). One important caveat applies throughout: b -value estimates are sensitive to the magnitude of completeness (M_c) of the underlying catalog, and careful M_c assessment is a necessary prerequisite for drawing meaningful conclusions. The background seismicity rate (μ) approaches the same problem from a complementary angle. By isolating the rate

of independent earthquake occurrence after systematic removal of aftershocks, foreshocks, and swarms through declustering, μ captures the component of seismicity most directly tied to ongoing tectonic stress accumulation Zaliapin and Ben-Zion (2013); van Stiphout et al. (2012). The rate-state friction framework provides a clear physical basis for this connection: as fault systems are loaded tectonically, background seismicity rates respond accordingly Hainzl et al. (2006); Heimisson and Segall (2018); Nandan et al. (2017). The observational record supports this interpretation. Large earthquakes tend to nucleate preferentially in regions of elevated background seismicity Ogata (2022), and variations in μ have been associated with independently measurable signals in crustal strain, transient stress fields, and subsurface fluid dynamics Stevens and Avouac (2021). What makes the joint use of these two parameters particularly attractive is that they are physically complementary rather than redundant. The b -value is primarily sensitive to the structural and stress-dependent organization of fault systems, while μ reflects the ambient intensity of tectonic loading. Together, they capture dimensions of fault system behavior that neither reveals in isolation. Regions where low b -values coincide with high background seismicity rates are of particular concern, as they identify fault segments that are both highly stressed and actively loaded, conditions broadly associated with proximity to failure. Where high b -values and low background rates co-occur, the picture is one of more heterogeneous and less critically stressed crustal volumes Ahadov and Ozturk (2022); Mousaviyan and Mostafazadeh (2025). This joint framework provides a physically grounded basis for spatial seismic hazard assessment in settings where fault complexity limits what any single parameter can usefully reveal. The Alborz Fold-Thrust Belt of northern Iran is one such setting. Shaped by the ongoing convergence of the Arabian and Eurasian plates at approximately 22 mm/yr, the belt accommodates deformation through a combination of reverse and strike-slip faulting along active structures that include the North Tehran, Mosha, and Khazar faults, among others Berberian and Yeats (1999); Tourani et al. (2024). The seismic consequences of this tectonic configuration are well documented. Among the most destructive regional events are the 2004 M_w 6.2 Baladeh earthquake and the 2010 M_w 5.9 Kuh-Zar earthquake Tatar et al. (2007); Gheitanchi (2005); Shahvar and Zare (2013). Continued investment in the Iranian national seismic network has produced catalogs of sufficient density and resolution to support detailed statistical seismicity analysis. Nevertheless, the joint spatial predictive value of the b -value and background seismicity rate has not been systematically evaluated within this tectonic setting, and that gap is what the present study directly addresses. In this study, μ refers to the background seismicity rate estimated after declustering within the Epidemic Type Aftershock Sequence (ETAS) framework. We map both parameters across the Alborz Fold-Thrust Belt, assess their individual and combined ability to forecast the spatial distribution of moderate to large earthquakes using the Molchan Error Diagram (MED), Probability Gain (PG), and Probability Difference (PD), and interpret the outcomes in the context of regional seismic hazard. The broader aim is to contribute to the methodological development of seismicity-based forecasting in tectonically complex environments where physically interpretable and statistically robust approaches are most needed. The remainder of this paper is organized as follows. Section 2 outlines the methodological framework and statistical procedures. Section 3 describes the seismic dataset and catalog preparation. Section 4 presents and discusses the forecasting results. Section 5 summarizes the principal findings and their implications for seismic hazard assessment in the Alborz region and comparable tectonic settings.

2 Methodology

2.1 b -Value Estimation and Spatial Mapping

The frequency–magnitude distribution of earthquakes is described by the classical Gutenberg–Richter (G–R) relation [Gutenberg and Richter \(1944\)](#):

$$\log_{10} N(M) = a - bM \quad (1)$$

where $N(M)$ is the cumulative number of earthquakes with magnitude greater than or equal to M , a reflects the regional seismic productivity, and b characterizes the relative occurrence of large to small events.

The b -value is estimated using the maximum likelihood method [Aki \(1965\)](#); [Wiemer and Wyss \(1997\)](#):

$$b = \frac{\log_{10} e}{M - M_c} \quad (2)$$

where \bar{M} is the mean magnitude of the earthquakes in the sample, and M_c is the magnitude of completeness. The associated standard error of the estimate is given by [Shi and Bolt \(1982\)](#):

$$\sigma_b = 2.30b^2 \sqrt{\frac{\sum_{i=1}^n (M_i - \bar{M})^2}{n(n-1)}} \quad (3)$$

The magnitude of completeness M_c is determined by the Maximum Curvature method [Wiemer and Wyss \(2000\)](#), defined as the magnitude bin with the highest frequency in the non-cumulative frequency–magnitude distribution.

To resolve the spatial variability of the b -value, we adopt the Hierarchical Space–Time Point-Process Model (HIST-PPM) framework [Ogata et al. \(2020\)](#). Under this framework, $\beta = b \ln(10)$ is treated as a spatially continuous field parameterized through a two-dimensional spline representation:

$$\beta(x, y) = \sum_{j=1}^m \theta_j B_j(x, y) \quad (4)$$

where θ_j denotes the spline coefficients and $B_j(x, y)$ represent the piecewise linear basis functions. The study region is tessellated into Delaunay triangular elements centered on earthquake epicenters, adaptively concentrating spatial resolution where seismicity is densest. To prevent overfitting, θ is estimated by maximizing the penalized log-likelihood:

$$\ln L_P(\theta) = \ln L(\theta) - \omega \Phi(\theta) \quad (5)$$

where $\ln L(\theta)$ is the point-process log-likelihood, $\Phi(\theta)$ is the spatial roughness penalty function, and ω is the smoothing hyperparameter. The roughness penalty weight ω is optimized by minimizing the Akaike Bayesian Information Criterion (ABIC):

$$\text{ABIC} = -2 \ln L_P(\hat{\theta}) + 2 \ln \det(\mathbf{H}_P(\hat{\theta})) - 2 \ln \det(\omega \mathbf{G}) + 2k \quad (6)$$

where $\hat{\theta}$ is the maximum penalized likelihood estimate, \mathbf{H}_P is the Hessian of the penalized log-likelihood, \mathbf{G} is the roughness penalty matrix, and k is the number of hyperparameters. Final b -values at epicenters are interpolated to a $0.1^\circ \times 0.1^\circ$ grid via linear interpolation within triangular elements.

2.2 Background Seismicity Rate

The spatially varying background seismicity rate $\mu(x, y)$ is estimated using the Epidemic-Type Aftershock Sequence (ETAS) model [Zhuang et al. \(2002\)](#), which decomposes the observed seismicity into a stationary background process and a triggered aftershock component. The total conditional seismic intensity $\lambda(t, x, y)$ is given by:

$$\lambda(t, x, y) = \mu(x, y) + \sum_{i:t_i < t} \kappa(M_i) g(t - t_i) f(x - x_i, y - y_i; M_i) \quad (7)$$

The aftershock productivity follows $\kappa(M_i) = K_0 e^{\alpha(M_i - M_c)}$, and the temporal decay is governed by the modified Omori–Utsu law:

$$g(t) = \frac{p-1}{c} \left(1 + \frac{t}{c}\right)^{-p} \quad (8)$$

All model parameters ($K_0, \alpha, c, p, d, q, \gamma$) are estimated by maximizing the log-likelihood over the observation window.

For each earthquake, the probability of belonging to the background process (the declustering probability) is calculated as:

$$\rho_i = \frac{\mu(x_i, y_i)}{\lambda(t_i, x_i, y_i)} \quad (9)$$

The background seismicity rate is then reconstructed via a variable-bandwidth Gaussian kernel estimator:

$$\mu(x, y) = \frac{1}{T} \sum_{i=1}^N \frac{\rho_i}{2\pi d_i^2} \exp\left(-\frac{(x - x_i)^2 + (y - y_i)^2}{2d_i^2}\right) \quad (10)$$

where T is the total observation period and the bandwidth d_i is the radius of the smallest circle centered at (x_i, y_i) enclosing at least $n_p = 3$ neighboring events, subject to a minimum threshold $\varepsilon = 0.02$. Estimation proceeds iteratively: the updated $\mu(x, y)$ is re-injected into the ETAS model and parameters are re-estimated until convergence [Zhuang et al. \(2002\)](#).

2.3 Evaluation of Forecast Performance

Forecast performance is evaluated using the Molchan Error Diagram [Molchan \(1990\)](#), which traces the relationship between the alarming rate (τ), defined as the fraction of grid cells placed under alarm, and the missing rate ($1 - \nu$), defined as the fraction of target earthquakes occurring outside alarmed cells. For the b -value, cells with $b < b_{\text{thr}}$ are alarmed; for the background rate, cells with $\mu > \mu_{\text{thr}}$ are alarmed. A forecast outperforming random guessing lies below the diagonal in the error diagram.

Two scalar metrics further quantify forecast skill. The Probability Gain (PG) is defined as:

$$\text{PG} = \frac{\nu}{\tau} \quad (11)$$

which measures the improvement in detection relative to a random alarm of equal size ($\text{PG} > 1$ indicates skill). The Probability Difference (PD) is defined as:

$$\text{PD} = \nu - \tau \quad (12)$$

alarm-based forecasts against a random spatial reference model. Across nearly the entire range of alarm rates τ , the curve for the background seismicity rate μ consistently falls well below the diagonal. This indicates that cells with elevated μ capture a disproportionately large share of target earthquakes while occupying only a modest fraction of the study area. Such behavior is fully consistent with physical expectations: μ reflects long-term tectonic loading and the persistence of fault activity, and its spatial concentration along active structures naturally makes it a strong predictor of future seismicity [Wiemer and Wyss \(2002\)](#); [Zechar and Jordan \(2010\)](#). The resulting probability gain reaches 5–6 at $\tau < 0.10$, demonstrating that a small subset of high- μ cells hosts earthquakes at rates several times higher than chance; an expression of the strong spatial clustering characteristic of the Alborz active fault system. The b -value behaves quite differently at these lower magnitude thresholds. For both $M \geq 4.0$ and $M \geq 4.5$, the b -value curve lies close to or above the diagonal, and its probability gain remains near unity. In other words, alarming low- b cells does not meaningfully outperform a random forecast for these magnitudes. This should not be interpreted as a failure of the b -value concept. Rather, it reflects well-known limitations in b -value estimation: the metric is most informative when target events are relatively large and sparse, and when the magnitude range lies comfortably above the completeness threshold [Schorlemmer et al. \(2005\)](#). Below roughly M_w 5.3, spatial instability in b -value estimation and residual completeness issues tend to obscure the stress-related signal. The negative probability difference values further confirm that, at these magnitudes, b -value alarms cover more area than they successfully identify as seismically active.

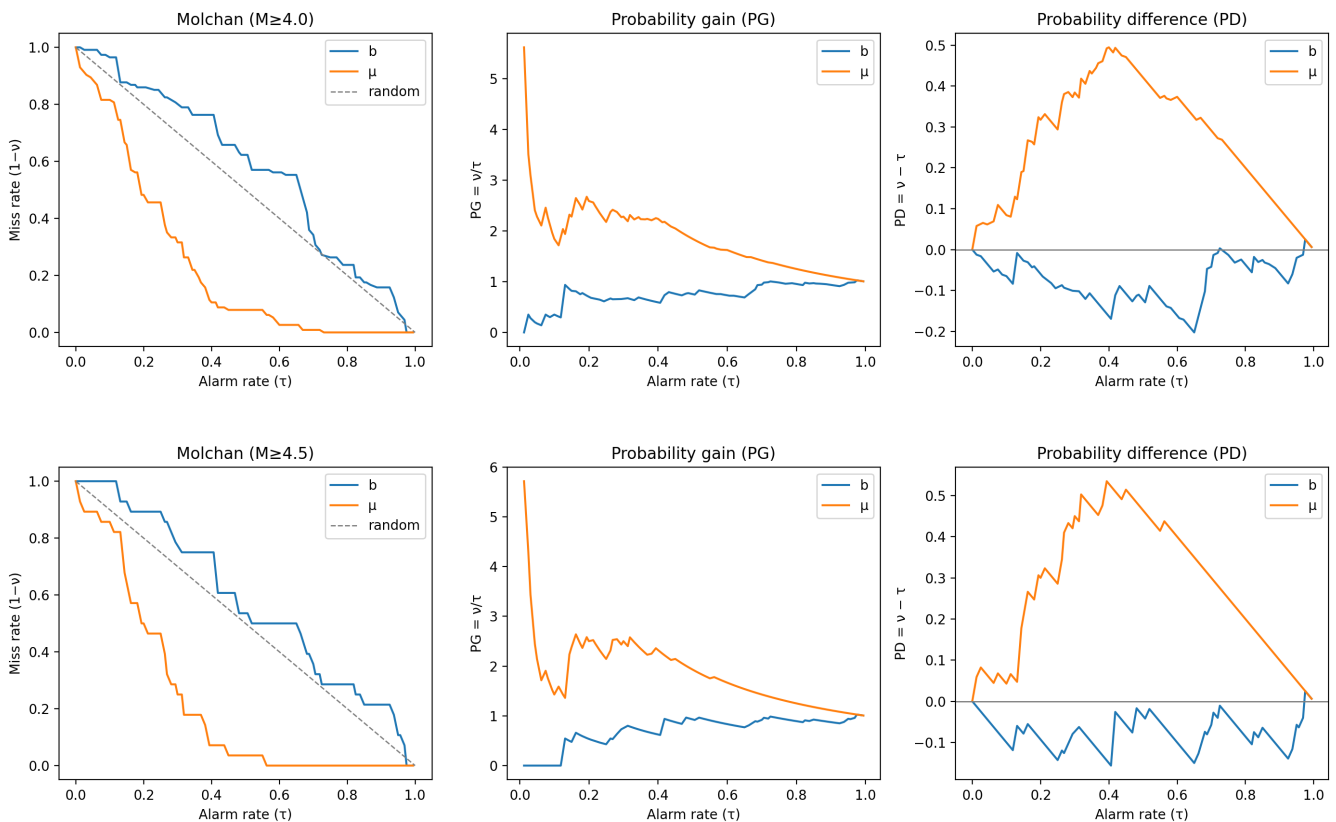


Figure 2 Molchan error curves, probability gain (PG), and probability difference (PD) for earthquakes with $M \geq 4.0$ and $M \geq 4.5$, illustrating the comparative forecasting performance of the b -value and background seismicity rate μ .

Figure 3 provides the clearest insight into the magnitude-dependent behavior of both predictors. By examining the maximum probability gain, maximum probability difference, and modified area skill score S as continuous

functions of magnitude, it reveals patterns that cannot be captured by a single alarm map or summary statistic. The probability gain results show a steady increase in b -value PG from ~ 1.0 at M_w 4.0 to ~ 2.5 at M_w 5.5. This trend is physically intuitive: as magnitude increases, target events become more strongly governed by long-term stress heterogeneity, and low- b anomalies become more reliable indicators of where larger events are likely to nucleate. The μ -based PG remains higher overall, reflecting its role as the stronger individual predictor, although the spike near $M \approx 5.1$ likely reflects a cluster of events that happened to fall within high- μ cells during the evaluation period. The probability difference panel reinforces this interpretation. The b -value PD rises monotonically from near zero at M_w 4.0 to ~ 0.6 at M_w 5.5, confirming that b -value heterogeneity becomes increasingly informative with magnitude. In contrast, μ shows a relatively stable PD (~ 0.50 – 0.65) across all thresholds, consistent with its magnitude-independent representation of tectonic loading. The convergence of b -value and μ PD values at $M \geq 5.5$ is particularly important: at magnitudes capable of causing structural damage, the two predictors become comparably informative and therefore highly complementary. The modified area skill score S completes the picture. The b -value S is negative at low magnitudes, crosses zero near $M \approx 5.3$, and becomes modestly positive at $M \geq 5.5$. This zero-crossing provides a natural operational threshold: below M_w 5.3, b -value information degrades forecast performance, whereas above this threshold it becomes a meaningful and physically grounded contributor. The μ -based S remains positive across all magnitudes, reaffirming its role as a stable, magnitude-agnostic spatial prior.

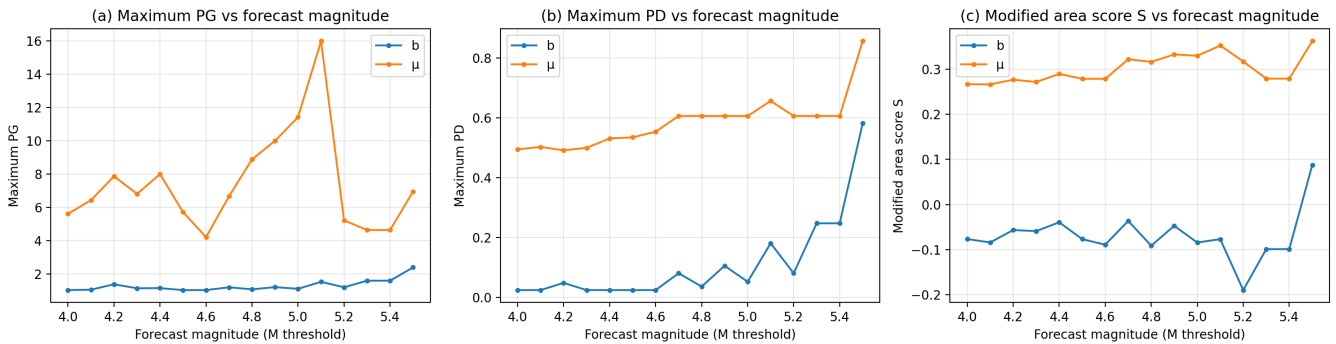


Figure 3 Forecasting performance of spatial b -value and background seismicity rate (μ) for 2025–2029 based on PG, PD, and S analyses.

Figure 4 explores how forecast skill evolves when the b -value and μ thresholds are varied jointly, presenting two-dimensional PG and PD surfaces across the full parameter space of combined alarm rates (τ_b, τ_μ) for $M \geq 4.5$ and $M \geq 4.0$. The PG surfaces confirm what one might expect from the individual results: the highest probability gains are achieved when both thresholds are simultaneously tightened, concentrating alarms in a very small fraction of the study area ($\tau_b < 0.15, \tau_\mu \approx 0$, bottom-left corner of the parameter space). This is encouraging from a physical standpoint: it means that the intersection of low- b and high- μ cells defines a genuinely high-hazard zone, not merely a region that happens to be large. The PD surfaces are arguably more useful for operational purposes, precisely because PD explicitly penalizes both missed events and unnecessary alarms. The PD extending across $\tau_b = 0.5$ – 1.0 and $\tau_\mu = 0.3$ – 0.6 indicates that the integrated forecast performs well not just at a single optimal point, but across a wide swath of the parameter space. This robustness means that the forecast conclusions are not hostage to precise threshold calibration. Looking at the background seismicity rate maps (Figure 5), the observation is that seismic activity in the Alborz is far from uniform. During 2006–2015 (Figure 5a), the highest μ values are found in the western

Figure 5: Combined Forecast Performance (τ_μ vs τ_b) with Rainbow Colormap

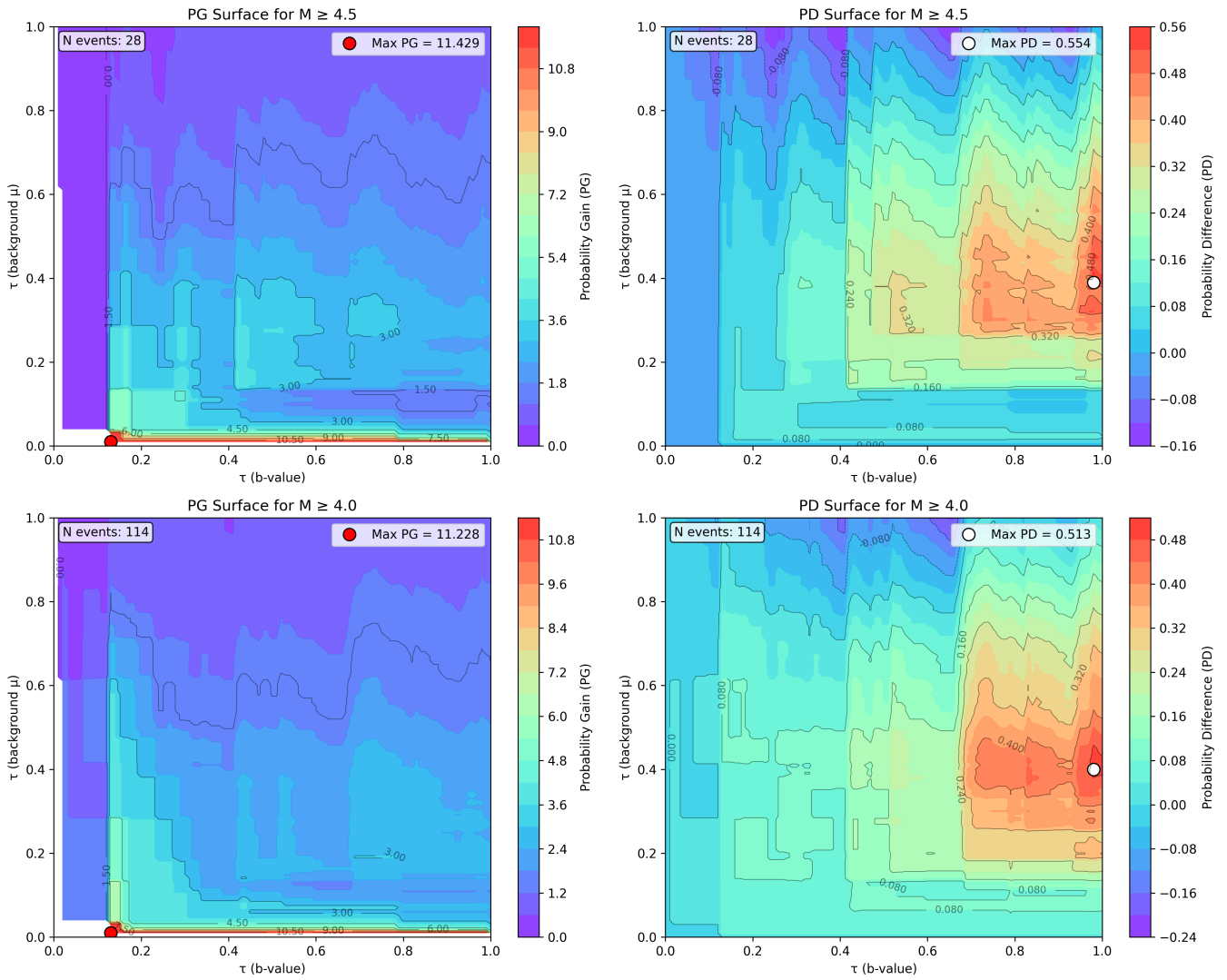


Figure 4 Forecast performance across the τ_b - τ_μ parameter space for $M \geq 4.5$ and $M \geq 4.0$ based on PG and PD metrics, highlighting different sensitivities of the two measures and the dependence of optimal model performance on threshold parameters.

Alborz, clustering around the Rudbar Fault Zone and the Soltaniyeh Fault, with a particularly pronounced hotspot near 49.5°E, 35.5°N. This concentration is hardly surprising given the long shadow cast by the 1990 M_w 7.4 Rudbar earthquake: even decades after a major rupture, background seismicity tends to remain elevated in its vicinity, reflecting ongoing stress redistribution and possibly fluid-driven reactivation along subsidiary structures Hainzl and Ogata (2005). What is more striking, however, is what happens in the following decade. By 2015–2024 (Figure 5b), the seismicity landscape reorganizes itself in a geographically meaningful way. A new zone of elevated μ emerges in the central-eastern Alborz, concentrated around the Astaneh and Atari faults (53°–54°E). The western concentration does not disappear, but it weakens relative to the new activity centers further east. This eastward migration of background seismicity likely reflects genuine changes in the regional stress field, possibly driven by progressive interseismic loading along the North Alborz fault system or by fluid migration at depth, mechanisms that have been documented in comparable compressional tectonic settings Hainzl and Ogata (2005). Figure 6 provides a distinct

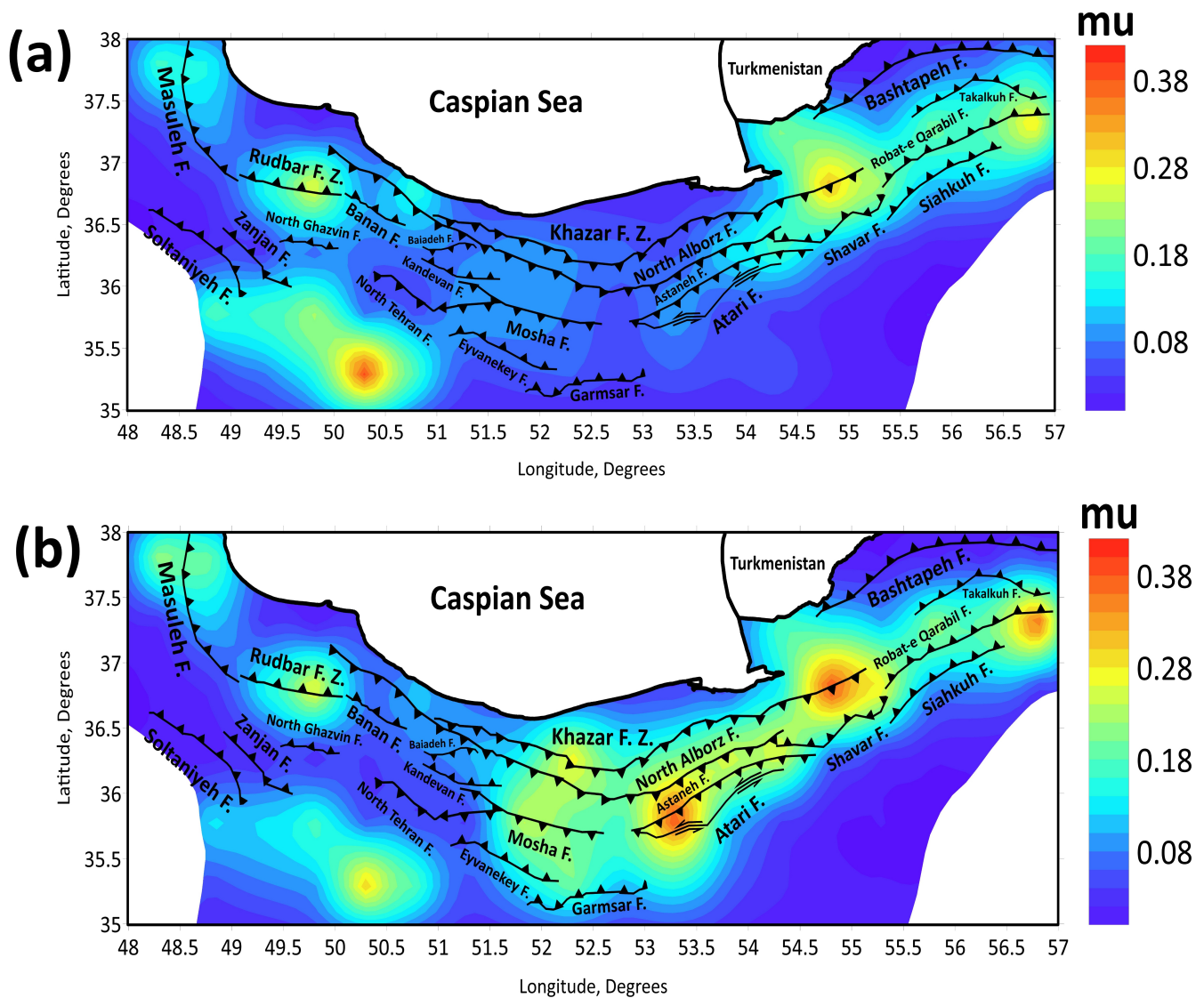


Figure 5 Spatial distribution of the background seismicity rate across the Alborz region for the periods (a) 2006–2015 and (b) 2015–2024. The maps illustrate temporal variations in background seismic activity derived from the ETAS framework.

yet complementary characterization of the physical state of the Alborz crust relative to other seismic indicators. Regions where the crust is being squeezed harder tend to produce proportionally more large earthquakes relative to

small ones, depressing the b -value Scholz (2015); Schorlemmer et al. (2005). During 2006–2015 (Figure 6a), the most stressed portions of the Alborz, as inferred from low b -values ($b < 0.8$), are concentrated in the western sector near the Soltaniyeh Fault and across the North Tehran and Eyvanekey fault zones. These are structurally complex zones where multiple fault strands interact under the broad NNE-directed compression imposed by Arabia–Eurasia convergence. The central Alborz shows intermediate b -values, and the eastern sector near the Bashtapeh and Siahkuh faults appears relatively relaxed, with higher b -values suggesting lower stress accumulation in that period. By 2015–2024 (Figure 6b), the western stress anomaly largely persists, but something new develops in the central Alborz: a broader low- b zone expands to encompass the Moshā and Kandevar fault systems. This spatial expansion of the stress anomaly suggests progressive strain accumulation across a broader portion of the range, a pattern consistent with geodetic evidence for distributed shortening along the Alborz Vernant et al. (2004). The eastern Alborz continues to exhibit moderately high b -values through this period, suggesting that it has not yet accumulated the level of stress loading seen further west. One particularly important observation emerges when the μ and b -value maps

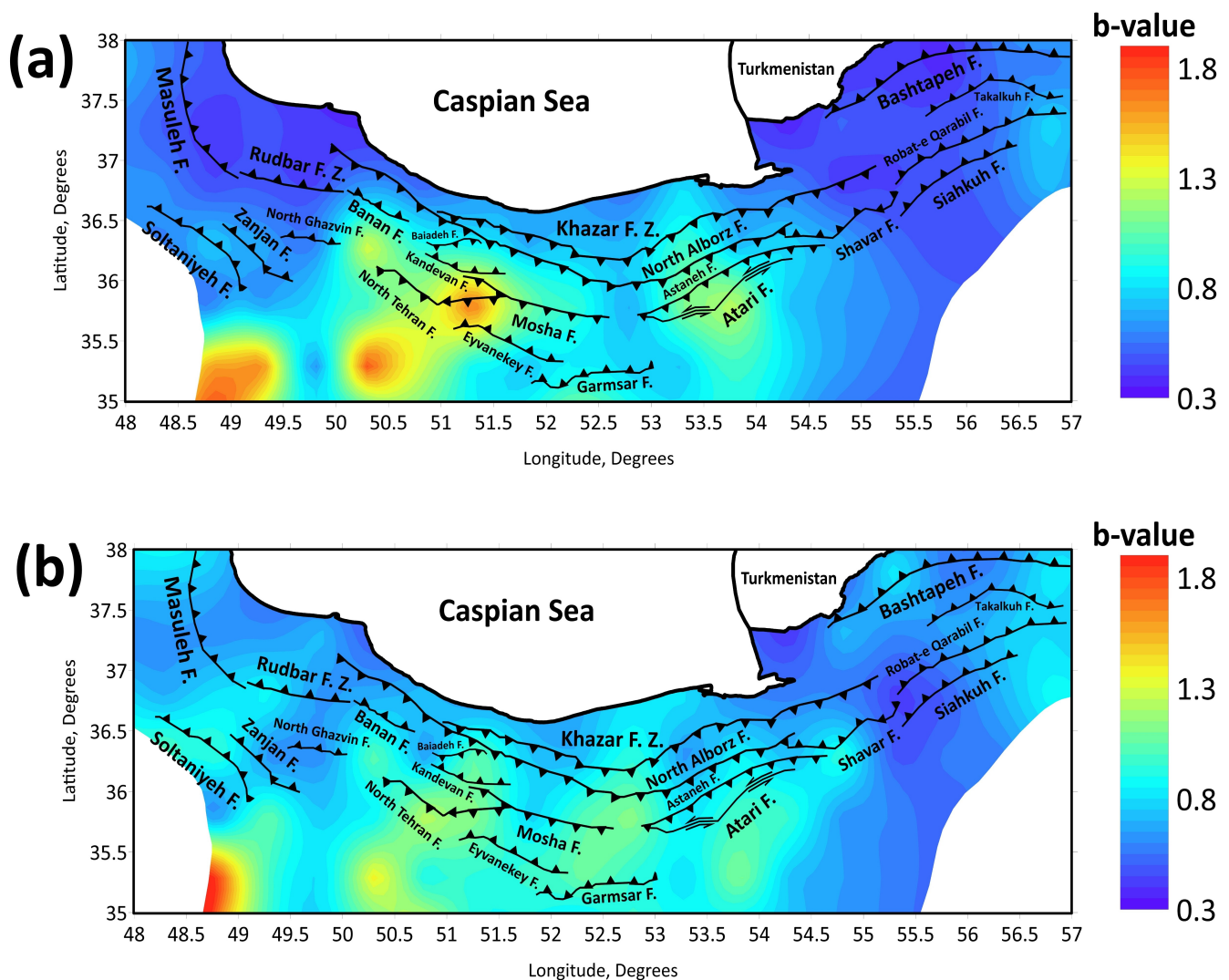


Figure 6 Spatial distribution of b -values for the periods (a) 2006–2015 and (b) 2015–2024.

are viewed side by side: they do not mirror each other. Regions of high background seismicity do not systematically coincide with regions of low b -value, and vice versa. This spatial decoupling is not a methodological inconsistency; it is precisely what one would expect if these two parameters are capturing different physical aspects of the seismo-

genic system. The b -value reflects the current stress state of the crust, while μ integrates the long-term structural capacity of a region to generate earthquakes. Zhang et al. (2025) similarly found no spatial correlation between μ and the b -value in Yunnan Province. They interpreted this lack of correlation as evidence that the two parameters provide complementary rather than overlapping information about the seismotectonic state. The same interpretation is equally applicable to the Alborz region. Figure 7 illustrates the spatial b -value distribution across the Alborz region for the 2015–2024 training period, together with the alarmed grid cells identified by applying the PD-optimized threshold. Panel (a) presents the b -value map with alarmed cells overlaid as red-bordered squares, and panel (b) translates this into a forward earthquake forecast for 2025–2029. The b -value map for 2015–2024 reveals a spatially heterogeneous stress field, with the most pronounced low- b anomalies ($b < 0.8$) concentrated in the western Alborz near the Soltaniyeh and Rudbar fault systems, secondary anomalies in the central Alborz around the Banan and Baladeh faults, and additional low- b patches in the northeastern sector encompassing the Bashtapeh, Robat-e Qarabil, and Siahkuh fault systems. Application of the PD-optimized threshold identifies five spatially compact alarmed clusters corresponding to these fault zones, reflecting the selective nature of the low- b criterion in targeting fault segments with the most compelling evidence of stress concentration. The forward forecast for 2025–2029 (Figure 7b) exhibits a substantially expanded alarm footprint relative to the training period. Four principal high-risk zones are identified:

1. the western Alborz, incorporating the Masulieh, Rudbar, Zanjan, and Soltaniyeh fault systems;
2. an extensive central Alborz band encompassing the North Tehran, Mosha, Kandeivan, Baladeh, and Khazar fault systems;
3. the eastern sector around the Astaneh and North Alborz faults ($\sim 52.5^\circ$ – 54° E), forming a spatial bridge between the central and northeastern clusters; and
4. the northeastern Alborz across the Bashtapeh, Robat-e Qarabil, and Siahkuh fault systems.

This spatial expansion reflects the broader low- b anomaly characterizing the 2015–2024 map and is physically consistent with geodetically observed distributed NNE-directed crustal shortening along the Alborz Vernant et al. (2004).

5 Conclusion

The background seismicity rate μ emerges as a consistently reliable spatial predictor across all tested magnitude thresholds ($M \geq 4.0$ and $M \geq 4.5$). Its strong performance reflects the direct physical connection between μ and long-term tectonic loading, fault architecture, and the persistence of seismic activity along structurally controlled zones. The stability of μ across magnitude thresholds further supports its value as a robust spatial prior in seismic hazard assessment. The b -value shows a clear and physically meaningful dependence on magnitude. At lower thresholds ($M < 5.3$), spatial variability in b -value estimates and their proximity to the completeness limit reduce their forecasting capability, which is reflected in negative skill scores and probability gains close to unity. Once magnitudes exceed approximately M_w 5.3, the skill score becomes positive and b -value anomalies begin to serve as informative indicators of crustal stress concentration and potential nucleation zones for larger earthquakes. This

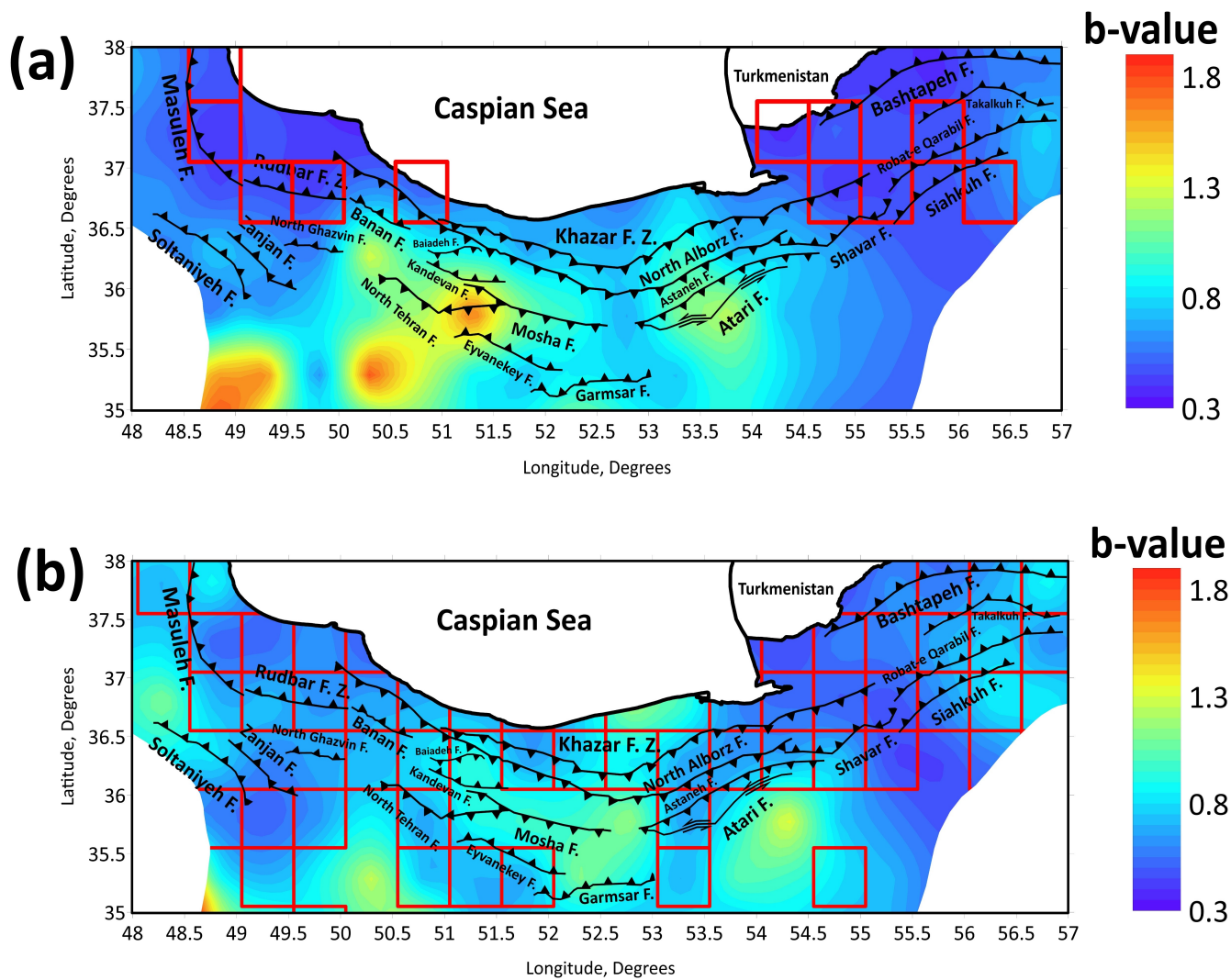


Figure 7 (a) Alarm areas predicted for the 2015–2024 period. (b) Forecasted alarm locations for the 2025–2029 interval.

magnitude-dependent transition provides a practical criterion for when b -value information can be reliably incorporated into probabilistic forecasting frameworks. A spatial comparison of b -value and μ distributions reveals only limited correlation, indicating that the two parameters capture fundamentally different physical aspects of earthquake generation. The b -value reflects the present differential stress state of the crust, whereas μ represents the long-term structural capacity of fault systems to sustain seismic activity. This spatial decoupling aligns with observations from other compressional tectonic settings and highlights the complementary, rather than redundant, nature of the two predictors. When combined within a unified forecasting framework, the b -value and μ outperform either predictor used independently. The prospective 2025–2029 spatial forecast, constructed from the 2015–2024 b -value map using the PD-optimized threshold, identifies four principal alarmed zones. Taken together, the integration of stress-sensitive and rate-based indicators within a single probabilistic model provides a more physically comprehensive and operationally effective approach to spatial earthquake forecasting. The 2025–2029 forecast offers a testable, time-bounded contribution to seismic hazard assessment in the Alborz and establishes a methodological foundation for future real-time and operational forecasting efforts in tectonically active regions.

Data Availability

The earthquake catalog used in this study was obtained from the Iranian Seismological Center (IRSC), Institute of Geophysics, University of Tehran (<https://irsc.ut.ac.ir/>). According to the data-use agreement required by the Institute of Geophysics, redistribution of the catalog and any processed or derivative datasets is not permitted. Therefore, the declustered catalog and derived seismicity parameters cannot be made publicly available. These materials may be shared privately upon reasonable request, provided such sharing complies with IRSC restrictions.

Acknowledgment

We gratefully acknowledge the Iranian Seismological Center (IRSC) for providing the comprehensive earthquake catalog used in this study, which was instrumental in conducting the spatiotemporal analysis of seismicity.

Declarations

Conflict of interest

The authors declare that they have no known competing financial interests or personal relationships that could have appeared to influence the work reported in this paper.

References

- Ahadov, B. and Ozturk, S. Spatial variations of fundamental seismotectonic parameters for the earthquake occurrences in the Eastern Mediterranean and Caucasus. *Natural Hazards*, 111(3):2177–2192, 2022. doi: 10.1007/s11069-021-05136-1.
- Aki, K. Maximum likelihood estimate of b in the formula $\log N = a - bM$ and its confidence limits. *Bulletin of the Earthquake Research Institute, University of Tokyo*, 43:237–239, 1965.
- Bakun, W. H. and Lindh, A. G. The Parkfield, California, earthquake prediction experiment. *Science*, 229(4714):619–624, 1985. doi: 10.1126/science.229.4714.619.

- Beall, A., van den Ende, M., Ampuero, J. P., Capitanio, F. A., and Fagereng, A. Linking Earthquake Magnitude-Frequency Statistics and Stress in Visco-Frictional Fault Zone Models. *Geophysical Research Letters*, 49(17):e2022GL099247, 2022. doi: 10.1029/2022GL099247.
- Berberian, M. and Yeats, R. S. Patterns of historical earthquake rupture in the Iranian Plateau. *Bulletin of the Seismological Society of America*, 89(1):120–139, 1999. doi: 10.1785/BSSA0890010120.
- Beroza, G. C., Segou, M., and Mousavi, S. M. Machine learning and earthquake forecasting—next steps. *Nature Communications*, 12:5056, 2021. doi: 10.1038/s41467-021-25375-3.
- Brodsky, E. E. Long-range triggered earthquakes that continue after the wave train passes. *Geophysical Research Letters*, 33(15):L15313, 2006. doi: 10.1029/2006GL026605.
- Cavallo, E., Powell, A., and Becerra, O. Estimating the Direct Economic Damage of the Earthquake in Haiti. Working Paper Series IDB-WP-163, Inter-American Development Bank, 2010.
- Convertito, V., Tramelli, A., and Godano, C. *b*-map evaluation and on-fault stress state for the Antakya 2023 earthquakes. *Scientific Reports*, 14(1):1596, 2024. doi: 10.1038/s41598-023-50837-3.
- Cui, P., Zhu, X.-H., Han, Y.-S., Chen, X.-Q., and Zhuang, J.-Q. The Wenchuan earthquake (May 12, 2008), Sichuan Province, China, and resulting geohazards. *Natural Hazards*, 56(1):19–36, 2011. doi: 10.1007/s11069-009-9489-1.
- El-Isa, Z. H. and Eaton, D. W. Spatiotemporal variations in the *b*-value of earthquake magnitude–frequency distributions: Classification and causes. *Tectonophysics*, 615–616:1–11, 2014. doi: 10.1016/j.tecto.2013.12.001.
- Geller, R. J., Jackson, D. D., Kagan, Y. Y., and Mulargia, F. Earthquakes cannot be predicted. *Science*, 275(5306):1616–1617, 1997. doi: 10.1126/science.275.5306.1616.
- Gheitanchi, M. R. Source characteristics of the 28th May 2004 Baladeh-Kojour destructive earthquake in Central Alborz, revealed from far field waveform data. *Scientific Quarterly Journal of Geosciences*, 14(55):154–163, 2005.
- Gutenberg, B. and Richter, C. F. Frequency of earthquakes in California. *Bulletin of the Seismological Society of America*, 34(4):185–188, 1944. doi: 10.1785/BSSA0340040185.
- Hainzl, S. and Ogata, Y. Detecting fluid signals in seismicity data through statistical earthquake modeling. *Journal of Geophysical Research: Solid Earth*, 110(B5):B05S07, 2005. doi: 10.1029/2004JB003247.
- Hainzl, S., Kraft, T., Wassermann, J., Igel, H., and Schmedes, E. Evidence for rainfall-triggered earthquake activity. *Geophysical Research Letters*, 33(19):L19303, 2006. doi: 10.1029/2006GL027642.
- Heimisson, E. R. and Segall, P. Constitutive law for earthquake production based on rate-and-state friction: Dieterich 1994 revisited. *Journal of Geophysical Research: Solid Earth*, 123(5):4141–4156, 2018. doi: 10.1029/2018JB015525.
- Jordan, T. H. and Jones, L. M. Operational earthquake forecasting: Some thoughts on why and how. *Seismological Research Letters*, 81(4): 571–574, 2010. doi: 10.1785/gssrl.81.4.571.
- Karimiparidari, S., Moinfar, A. A., and Maleki, M. Iranian earthquakes, a uniform catalog with moment magnitudes. *Journal of Seismology*, 17(3):897–911, 2013. doi: 10.1007/s10950-013-9360-y.
- Kazama, M. and Noda, T. Damage statistics (summary of the 2011 off the Pacific coast of Tohoku earthquake damage). *Soils and Foundations*, 52(5):780–792, 2012. doi: 10.1016/j.sandf.2012.11.003.
- Keilis-Borok, V. I. and Kossobokov, V. G. Premonitory activation of earthquake flow: Algorithm M8. *Physics of the Earth and Planetary Interiors*, 61(1-2):73–83, 1990. doi: 10.1016/0031-9201(90)90096-G.
- King, G. C. P., Stein, R. S., and Lin, J. Static stress changes and the triggering of earthquakes. *Bulletin of the Seismological Society of America*, 84(3):935–953, 1994. doi: 10.1785/BSSA0840030935.

- Lamessa, G., Mammo, T., and Raghuvanshi, T. K. Homogenized earthquake catalog and b -value mapping for Ethiopia and its adjoining regions. *Geoenvironmental Disasters*, 6(1):16, 2019. doi: 10.1186/s40677-019-0131-y.
- Michael, A. J., McBride, S. K., Hardebeck, J. L., Barall, M., Martinez, E., Page, M. T., and Wein, A. M. Statistical Seismology and Communication of the USGS Operational Aftershock Forecasts for the 30 November 2018 M_w 7.1 Anchorage, Alaska, Earthquake. *Seismological Research Letters*, 91(1):153–173, 2020. doi: 10.1785/0220190173.
- Molchan, G. M. Strategies in strong earthquake prediction. *Physics of the Earth and Planetary Interiors*, 61(1-2):84–98, 1990. doi: 10.1016/0031-9201(90)90097-H.
- Mousaviyan, S. and Mostafazadeh, M. Evaluation of seismic stress changes in the northern part of the Zagros in Iran. *Acta Geophysica*, 73(3):2245–2267, 2025. doi: 10.1007/s11600-025-01532-6.
- Nandan, S., Ouillon, G., Wiemer, S., and Sornette, D. Objective estimation of spatially variable parameters of Epidemic Type Aftershock Sequence model: Application to California. *Journal of Geophysical Research: Solid Earth*, 122(7):5118–5143, 2017. doi: 10.1002/2016JB013843.
- Nanjo, K. Z., Hirata, N., Obara, K., and Kasahara, K. Decade-scale decrease in b value prior to the M_9 -class 2011 Tohoku and 2004 Sumatra quakes. *Geophysical Research Letters*, 39(20):L20304, 2012. doi: 10.1029/2012GL052997.
- Nanjo, K. Z., Izutsu, J., Orihara, Y., and Kamogawa, M. Changes in seismicity pattern due to the 2016 Kumamoto earthquake sequence and implications for improving the foreshock traffic-light system. *Tectonophysics*, 822:229175, 2022. doi: 10.1016/j.tecto.2021.229175.
- Ogata, Y. Prediction and validation of short-to-long-term earthquake probabilities in inland Japan using the hierarchical space–time ETAS and space–time Poisson process models. *Earth, Planets and Space*, 74(1):114, 2022. doi: 10.1186/s40623-022-01673-8.
- Ogata, Y., Katsura, K., Tanemura, M., Harte, D., and Zhuang, J. Hierarchical Space-Time Point-Process Models (HIST-PPM): Software documentation. Software documentation, 2020. Available online at <https://bemlar.ism.ac.jp/ogata/HIST-PPM-V3/manual.pdf>.
- Sarlis, N. V., Skordas, E. S., Varotsos, P. A., Nagao, T., Kamogawa, M., and Uyeda, S. Spatiotemporal variations of seismicity before major earthquakes in the Japanese area and their relation with the epicentral locations. *Proceedings of the National Academy of Sciences*, 112(4):986–989, 2015. doi: 10.1073/pnas.1422893112.
- Scholz, C. H. On the stress dependence of the earthquake b value. *Geophysical Research Letters*, 42(5):1399–1402, 2015. doi: 10.1002/2015GL063222.
- Schorlemmer, D., Wiemer, S., and Wyss, M. Variations in earthquake-size distribution across different stress regimes. *Nature*, 437(7058):539–542, 2005. doi: 10.1038/nature04094.
- Shahvar, M. P. and Zare, M. The 27 August 2010 M_w 5.7 Kuh-Zar earthquake (Iran): Field investigation and strong-motion evidence. *Natural Hazards*, 66(2):689–706, 2013. doi: 10.1007/s11069-012-0507-6.
- Shi, H., Meng, L., Zhang, X., Chang, Y., Yang, Z., Xie, W., Hattori, K., and Han, P. Decrease in b value prior to the Wenchuan earthquake (M_s 8.0). *Chinese Journal of Geophysics*, 61(5):1874–1882, 2018. doi: 10.6038/cjg2018L0199.
- Shi, Y. and Bolt, B. A. The standard error of the magnitude-frequency b value. *Bulletin of the Seismological Society of America*, 72(5):1677–1687, 1982. doi: 10.1785/BSSA0720051677.
- Stevens, V. L. and Avouac, J. P. On the relationship between strain rate and seismicity in the India-Asia collision zone: Implications for probabilistic seismic hazard. *Geophysical Journal International*, 226(1):220–245, 2021. doi: 10.1093/gji/ggab096.
- Tatar, M., Jackson, J., Hatzfeld, D., and Bergman, E. The 2004 May 28 Baladeh earthquake (M_w 6.2) in the Alborz, Iran: Overthrusting the South Caspian Basin margin, partitioning of oblique convergence and the seismic hazard of Tehran. *Geophysical Journal International*, 170(1):249–261, 2007. doi: 10.1111/j.1365-246X.2007.03386.x.

- Tourani, M., Isik, V., Saber, R., Caglayan, A., and Chitea, F. Evaluation of seismicity and seismotectonics in the Alborz Mountains: Insights from seismic parameters, Northern Iran. *Journal of Seismology*, 28(3):675–706, 2024. doi: 10.1007/s10950-024-10204-5.
- van Stiphout, T., Zhuang, J., and Marsan, D. Seismicity Declustering. *Community Online Resource for Statistical Seismicity Analysis*, pages 1–25, 2012. doi: 10.62687/corssa-44589886.
- Vernant, P., Nilforoushan, F., Chery, J., Bayer, R., Djamour, Y., Masson, F., Nankali, H., Martinod, J., and Tavakoli, F. Deciphering oblique shortening of central Alborz in Iran using geodetic data. *Earth and Planetary Science Letters*, 223(1-2):177–185, 2004. doi: 10.1016/j.epsl.2004.04.017.
- Wang, Y. C., Mora, P., Yin, C., and Place, D. Statistical tests of load–unload response ratio signals by lattice solid model: Implication to tidal triggering and earthquake prediction. *Pure and Applied Geophysics*, 161(9):1829–1839, 2004. doi: 10.1007/s00024-004-2534-1.
- Wiemer, S. and Wyss, M. Mapping the frequency–magnitude distribution in asperities: An improved technique to calculate recurrence times. *Journal of Geophysical Research: Solid Earth*, 102(B7):15115–15128, 1997. doi: 10.1029/97JB00726.
- Wiemer, S. and Wyss, M. Minimum magnitude of completeness in earthquake catalogs: Examples from Alaska, the western United States, and Japan. *Bulletin of the Seismological Society of America*, 90(4):859–869, 2000. doi: 10.1785/0119990114.
- Wiemer, S. and Wyss, M. Mapping spatial variability of the frequency-magnitude distribution of earthquakes. In *Advances in Geophysics*, volume 45, pages 259–322. Elsevier, 2002. doi: 10.1016/S0065-2687(02)80007-3.
- Zaliapin, I. and Ben-Zion, Y. Earthquake clusters in southern California I: Identification and stability. *Journal of Geophysical Research: Solid Earth*, 118(6):2847–2864, 2013. doi: 10.1002/jgrb.50179.
- Zechar, J. D. and Jordan, T. H. Simple smoothed seismicity earthquake forecasts for Italy. *Annals of Geophysics*, 53(3):99–105, 2010. doi: 10.4401/ag-4845.
- Zhang, Y., Wang, R., Shi, H., Miao, M., Zhuang, J., Chang, Y., Hattori, K., and Han, P. Earthquake forecasting based on *b* value and background seismicity rate in Yunnan Province, China. *Entropy*, 27(2):205, 2025. doi: 10.3390/e27020205.
- Zhuang, J., Ogata, Y., and Vere-Jones, D. Stochastic declustering of space–time earthquake occurrences. *Journal of the American Statistical Association*, 97(458):369–380, 2002. doi: 10.1198/016214502760047008.